JOURNAL OF THERMOPHYSICS AND HEAT TRANSFER
Vol. 19, No. 3, July–September 2005

Investigation of Soot Combustion in Underexpanded Jet Plume Flows

K. Viswanath,* K. S. Brentner,† S. F. Gimelshein,‡ and D. A. Levin§
Pennsylvania State University, University Park, Pennsylvania 16802

A new overlay technique to model and simulate the soot combustion in rocket plumes is proposed and examined. An efficient methodology for the accurate prediction of soot oxidation is discussed so that the sensitivity of soot combustion to the complex plume flow characteristics may be better understood. The accurate prediction of soot combustion in rocket plumes affects the plume radiation pattern and the location of the maximum radiation in underexpanded rocket plumes. A continuum approach for the soot overlay problem is presented for the example problem of a single-nozzle axisymmetric plume representative of the Atlas rocket. The overlay calculations are applied to a third-order-accurate converged Navier–Stokes result for a chemically reacting gas flow at the altitudes of 21, 30, and 40 km. Results are presented to demonstrate the sensitivity of soot oxidation to the initial spatial distribution of soot at the nozzle exit plane and the altitude dependence of soot combustion in the plume flowfield for various pressure ratios. It is shown that the majority of the soot combustion occurs in the plume shear layer due to the higher temperatures and penetration of oxygen into the flow. Also, there is more combustion at lower altitudes due to increased availability of oxygen for combustion, even though the shear layer at the lower altitudes is thin.

Nomenclature

C_M	=	jet factor
D_e	=	nozzle exit diameter
f	=	reaction probability
k_r	=	total emission coefficient
L_{pl}	=	plume length
m_p	=	mass of a single soot particle
$\tilde{m}$	=	mass removed per second
N_s	=	soot number density
n	=	gas number density
p_c	=	chamber pressure
p_e	=	jet exit pressure
p_{inf}	=	ambient pressure
p_{O_2}	=	partial pressure of oxygen
q	=	vector of primitive variables
$q_{nr,i}$	=	energy transferred to soot particle by nonreactive collisions
$q_{r,i}$	=	energy transferred to soot particle by reactive collisions
r_i^+, r_i^-	=	ratios of solution differences
r_s	=	soot particle radius
T	=	temperature of the soot particle
T_{gas}	=	gas temperature
u	=	local velocity of the plume gas
u_i	=	solution at ith point
u_{i+1}	=	solution at $(i+1)$th point
u_{i-1}	=	solution at $(i-1)$ point
u_r	=	plume velocity in the radial direction
u_s	=	local velocity of soot fluid particle
u_x	=	plume velocity in the axial direction
u'	=	thermal velocity
Z	=	total collision frequency
ρ_p	=	density of the soot particle
ρ_s	=	density of soot
σ	=	Stefan–Boltzmann constant
ω	=	oxidation rate
ω_s	=	rate of soot production (or destruction) due to chemical reactions

I. Introduction

IMPORTANT fundamental investigations of the underlying physics and aerothermodynamics of rocket exhaust plumes encompasses research in propulsion, fluid dynamics, and radiation. The phenomenology of rocket exhaust plumes can provide guidance for the design and optimization of optical sensors for target detection, identification, and tracking. For this reason, an understanding of the influence of different parameters on the flow structure, such as the nozzle dimensions, chamber-to-ambient pressure ratio, vehicle velocity, and soot obscuration, as well as radiation signatures, is needed. Interaction of rocket plumes with the ambient atmosphere involves such complex gasdynamics phenomena as the formation of Mach disks, barrel shocks, and shear layer interactions. Accurate modeling of these phenomena in rapidly expanding plume exhaust flows is often complicated by the flow three dimensionality, turbulence, and chemical reactions. An additional problem that may obscure comparison of modeling and simulation results with experimental data is the presence in the plume of soot particles. Soot may contribute strongly to the optical radiation resulting from the plume–atmosphere interaction, although it is present in small quantities. The main goal of this work is to introduce an efficient overlay numerical technique to simulate the combustion of soot particles in rocket plumes so that the impact of the plume flow characteristics on the soot steady-state spatial distribution may be understood. In particular, the rocket plumes of interest are challenging to model and compute. They are multiphase, high-temperature, viscous, chemically reacting flows with large variations in length scales over the freestream conditions of interest. Our goal is to compute an accurate plume flowfield for the gaseous species only. The

Presented as Paper 2004-1350 at the AIAA 42nd Aerospace Sciences Meeting and Exhibit, Reno, NV, 5–8 January 2004; received 20 August 2004; revision received 4 November 2004; accepted for publication 5 November 2004.

*Graduate Research Assistant, Department of Aerospace Engineering; kamalv@psu.edu. Member AIAA.

†Associate Professor, Department of Aerospace Engineering; ksbrentner@psu.edu. Member AIAA.

‡Research Professor, Department of Aerospace Engineering; currently Department of Aerospace and Mechanical Engineering, University of Southern California, Los Angeles, CA; gimelshe@usc.edu. Member AIAA.

§Associate Professor, Department of Aerospace Engineering; dalevin@psu.edu. Associate Fellow AIAA.

overlay technique used to model the gas–soot particulate interaction should retain the accuracy of the original gas plume flowfield while at the same time should provide the comptutational efficiency to test different soot models.

Underexpanded jet flowfields have been extensively studied in the past. (See, for example, Ref. 1 and references therein.) It was shown by Moran[2] that for cold underexpanded jets the plume length can serve as a similarity quantity that depends on the geometry of the rocket nozzle and freestream conditions. The plume length $L_{\rm pl}$ is usually defined as the distance from the nozzle exit to to the reflection point of the barrel shock with the axis of symmetry. The jet factor, defined as

$$C_M = (L_{\rm pl}/D_e)\left(1\Big/\sqrt{p_e/p_\infty}\right) \tag{1}$$

is constant for a fixed nozzle and freestream Mach number. Here, p_e and p_∞ are the jet exit and ambient pressures, respectively. This relationship has been validated by the flow visualization experiments for cold underexpanded jets exhausting into a supersonic freestream performed by Bannik et al.[3] Morris et al.[4] obtained the following expression for the plume length:

$$L_{\rm pl} = \sqrt{p_c/p_\infty}D_e \tag{2}$$

A modified method of characteristics was developed and used by Genkin et al.[5] to predict the location and radius of the Mach disk as the function of the chamber-to-ambient pressure ratio for a constant specific heat ratio. The results of Genkin et al.[5] agree with Eq. (2). However, an accurate prediction of the plume length in a chemically reacting gas is a much more complicated problem that requires the numerical solution of the Navier–Stokes equations.

Understanding the correlation between the engine parameters and the location and the magnitude of the peak radiation in chemically reacting plumes is a challenging and important problem. The location of the radiation peak observed by passive sensors may provide valuable information about the engine properties, but could generally be different from the traditionally defined plume length.

To correlate engine performance with plume length, a number of specific topics need to be considered. The location of the radiation peak could be obtained from numerical solution of the Navier–Stokes equations for different chamber pressures, fuel-to-oxidizer ratios, and freestream velocities. In addition, the influence of the vehicle base flow on the near-field plume structure should also be considered. Previous studies by Ebrahimi et al.[6] and Alexeenko et al.[7] of the vehicle–plume interaction showed that the base flow may significantly affect the location of the barrel shock reflection. Finally, the inclusion of soot oxidation in the flow modeling may perhaps be the greatest factor needed to account for the obscuration of the true plume length and flow structure in radiation images. It is the last aspect that will be considered in this work.

Modeling of the soot transport, oxidation, and possible radiation effects has been studied by several researchers. Here we mention some of the recent work in the field. A model for the soot oxidation was proposed by Hiers[8,9] that, for the first time, used an approach based on the free-molecular, instead of the continuum, assumption. This model was used by Plastinin et al.[10] to study the soot oxidation in Atlas II rocket plumes approximated by a single-equivalent nozzle at 15 and 40 km using an overlay approach. The subsequent work of Karabadzhak et al.[11] used a more sophisticated technique with a full coupling of the gas and soot particles. The detailed comparison between the numerical and flight data for the Atlas II radiation spectra at altitudes between 20 and 50 km is given by Plastinin et al.,[12] who found that soot oxidation substantially impacts the plume radiative properties at lower flight altitudes.

In this work, we study the soot oxidation dependence on the degree of mixing of freestream molecular oxygen into the plume as a function of altitude. This work builds on the initial work presented by Brentner et al.[13] Two numerical techniques were applied by Brentner et al.,[13] where the model by Hiers[8] was used with continuum and kinetic approaches. For this paper, the soot combustion data from the continuum approach, which uses an overlay method to calculate soot distribution, is used. The plume flowfield was calculated solving the Reynolds-averaged Navier–Stokes with the general aerodynamics simulation program (GASP).[14]

A single-nozzle axisymmetric plume that is representative of the three-nozzle plume configuration of the Atlas rocket has been modeled. The Atlas plume is formed by a 40-kN kerosene/liquid oxygen (LOX) thruster. Such a plume can be computed because the thermochemical plume database is well established, and there exist experimental observations for this type of thruster. The soot oxidation rates obtained from the work of Hiers[8,9] will be applied. The soot particles distribution is obtained by using an overlay approach with specification of the concentration and the size of soot particles at the nozzle exit plane. Both particle and continuum overlay procedures exist, and the continuum overlay method and results are presented in this paper.

II. Soot Combustion

Carbon soot is produced by hydrocarbon fuels such as RP-1 and other kerosene like fuels that burn with oxidizers such as inhibited red fuming nitric acid or LOX. Soot found in the exhaust of the rocket plume comprises condensed, solid particles with diameters on the order of 20–200 nm. Because its dimension is much larger than the molecular size, it radiates in the optical spectral region as a graybody with the specific magnitude of radiation depending on the particle size and number density distribution in the plume. The specific mechanism for soot production, as well as the ability to predict the generated soot size and number distribution as a function of propellant and engine type, is qualitatively known at this time. The work of Wolfhard and Garcia[15] has shown that for operating pressures and temperatures typical of rocket engines soot production is enhanced in RP-1/O_2 propellants for fuel-rich mixtures. Rocket nozzle flow modeling usually assumes that the fuel-to-oxidizer ratio in a liquid propellant engine is spatially uniform. In a real system, the injector is usually designed to produce a uniform mixture ratio in the central region of the combustion chamber, but with a richer mixture near the wall. To some extent this nonuniformity in the oxidizer-to-fuel ratio will persist through the nozzle and into the plume flow.[1]

Hiers discusses a model for soot combustion that accounts for the Knudsen number based on particle diameter being large and for the gas flow about a soot particle being in the free-molecular regime.[9] By the use of a kinetic approach, the oxidation rate ω may be expressed as a fraction of the total number of collisions,

$$\omega = Zf\tilde{m} \tag{3}$$

where $\tilde{m}$ is the mass removed per reactive collision. Hiers shows that one may obtain an ordinary differential equation for the particle radius,

$$\frac{{\rm d}r_s}{{\rm d}t} = -\frac{Zf\tilde{m}}{\rho} \tag{4}$$

It has been assumed in this work that the dominant combustion reaction of soot is

$$2{\rm C} + {\rm O}_2 \rightarrow 2{\rm CO} \tag{5}$$

Combustion rates for soot oxidation by atomic oxygen and OH are available,[8] but these processes have not been included here because the concentrations of O and OH in the plume shear layer are lower than molecular oxygen and because of the uncertainties in the chemical rates for these processes. For the chemical combustion reaction (5), the total collision frequency may be expressed as

$$Z = \tfrac{1}{4}nu' \tag{6}$$

where n and u' are the gas number density and thermal velocity. The reaction probability is

$$f = \frac{\omega}{Z\tilde{m}} = \frac{12}{Z\tilde{m}}\left[\left(\frac{k_A p_{\rm O_2}}{1 + k_Z p_{\rm O_2}}\right)\chi + k_B p_{\rm O_2}(1-\chi)\right] \tag{7}$$

where

$$\chi = \left(1 + k_T/k_B p_{O_2}\right)^{-1}$$

$$k_A = 20\exp(-15{,}100/T), \qquad \text{g/(cm}^2 \cdot \text{s} \cdot \text{atm)}$$

$$k_B = 0.2\exp(-7640/T), \qquad \text{g/(cm}^2 \cdot \text{s} \cdot \text{atm)}$$

$$k_T = 1.51 \times 10^5 \exp(-48{,}800/T), \qquad \text{gm/(cm}^2 \cdot \text{s)}$$

$$k_Z = 21.3\exp(2060/T), \qquad \text{atm}^{-1}$$

The change of the soot particle temperature with time may be written as[8]

$$\frac{\mathrm{d}T}{\mathrm{d}t} = \frac{3}{\rho r C}\sum_i Z_i[f_i q_{r,i} + (1-f_i)q_{nr,i}] + \frac{3k_r\sigma}{\rho C}\left(T_{\text{gas}}^4 - T^4\right) \quad (8)$$

The summation is performed over molecular species i colliding with soot particles, where C is the specific heat of soot, and $q_{r,i}$ and $q_{nr,i}$ are the energies transferred to a soot particle by reactive and nonreactive collisions, respectively. The third term in Eq. (8) is related to the radiation heat transfer.

III. Soot Overlay Method

The soot concentration in plumes is usually low (typically much less than 1%); hence, it is expected that the soot does not affect the fluid dynamics or chemical kinetics mechanisms of the plume flow. Given this situation, an efficient computational approach is to separate the computation of the plume flow from that of the soot. The modeling of the soot species behavior using an overlay approach is suitable for most plume calculations. The overlay approach implies that the plume gas flowfield is calculated first; then the macroparameters of the plume such as density, velocity, and temperature are used to obtain a solution for the soot particle size, temperature, and spatial distribution throughout the plume.

Two approaches may generally be employed to calculate the soot properties. The first is the kinetic approach that takes into account the microscopic nature of the problem, and the second is an approach in which the soot is assumed to be governed by the continuum relationship for continuity. The comparison of the two methods was made in the previous work by Brentner et al.[13] The direct simulation Monte Carlo (DSMC) based overlay technique is computationally intensive compared to the continuum overlay approach presented in the next section, but it has several important advantages. First, it is applicable for modeling of soot combustion for any soot density, as long as the overlay assumption is valid. Second, the binary collisions of soot particles resulting in soot agglomeration may easily be included in the model. Third, the approach may be extended to take into consideration the variation in shape and size of different soot particles. Finally, information on the microscopic level is available from DSMC simulations, such as the particle velocity and size distribution functions.

An important observation obtained by using the DSMC-overlay approach for the conditions of interest in this work was that the soot particle velocities and temperatures exhibit only a small deviation from those of the plume background gas. Because the typical deviation did not exceed 0.1% of the magnitude for these properties in the entire flowfield, we concluded that the soot particles may be modeled to be following the plume gas particles with surface temperature and velocity equal to the local gas temperature and velocity. These observations justified the significantly simplified approach taken in the continuum algorithm presented hereafter.

The use of the overlay technique also allows us to take advance of significant computational savings. Because the DSMC studies[13] showed that the soot particles have the same velocity as the gas, the soot could have been modeled directly with the gas flow in the solution of the Navier–Stokes equations. However, given again that the criteria for utilizing the overlay method are met, the former approach would not be as computationally efficient as the overlay method. This is because the solution of the full Navier–Stokes equations scales approximately as the square of the number of equations being solved.[16] Apart from the savings of solving fewer chemical reactions in the main flow, the convergence is slow due to grid requirements, as will be discussed further in Sec. IV. Therefore, by using the overlay approach, we can concentrate on testing and understanding different soot combustion cases with a rapid, efficient algorithm that will be discussed in Sec. III.B without having to resolve the difficult plume flow for each case.

A. Continuum Overlay Approach

In the continuum overlay approach, the soot particles are assumed to act as a continuous "fluid" or species. The soot is assumed to have negligible interaction with itself and is not charged. The soot species is governed by a simple mass conservation law, which can be written in Eulerian form as

$$\frac{\partial \rho_s}{\partial t} + \nabla \cdot (\rho_s \boldsymbol{u}_s) = w_s \quad (9)$$

where ρ_s is the density of the soot fluid particle, $\boldsymbol{u}_s$ is the local velocity of the soot fluid particle, and w_s is the rate of soot production (or destruction) due to chemical reactions. (A soot fluid particle is distinctly different from a soot particle. A soot fluid particle refers to particle of continuum fluid that is, at the microscopic level, actually a collection of individual soot particles.) Similar statements of momentum and energy conservation could also be derived for the soot fluid; however, the observation that the soot velocity and surface temperature do not differ significantly from the plume gas flow eliminates the need for such equations. With the assumption $\boldsymbol{u}_s \approx \boldsymbol{u}$, where $\boldsymbol{u}$ is the local velocity of the plume gas, the subscript s can be dropped from $\boldsymbol{u}$ in Eq. (9). The relationship between source term w_s and the rate of change of soot particle radius given in Eq. (4) will be established later.

Although it would be natural to solve directly for ρ_s in Eq. (9), the computation of radiance requires both the soot number density N_s and soot particle radius r_s, individually. Soot density, number density, and particle radius are related by

$$\rho_s = N_s m_p \quad (10)$$

where N_s is the number of soot particles per unit volume and ρ_s is the soot fluid mass per unit volume. All soot particles in a soot fluid particle are assumed to have the same mass m_p, which is

$$m_p = \rho_p \tfrac{4}{3}\pi r_s^3 \quad (11)$$

for a spherical soot particle. Here, $\rho_p = 1950$ kg/m^3 [which is ρ in Eq. (8)].

Next, it is assumed that soot particles may have zero radius but cannot be created or destroyed; thus, the number density N_s accounts for the location of the soot particles, and the change in radius r_s of the particles accounts for any combustion of the soot. Hence, this model will yield zero soot density ($\rho_s = 0$) either when there are no soot particles in a region ($N_s = 0$) or if the soot has been completely consumed by oxidation ($r_s = 0$). Given this premise, the soot number density N_s must obey the conservation law,

$$\frac{\partial N_s}{\partial t} + \nabla \cdot (N_s \boldsymbol{u}) = 0 \quad (12)$$

The determination of N_s can be preformed independently from the computation of soot particle radius r_s. Furthermore, by using Eqs. (10) and (12) in Eq. (9), we find that m_p must satisfy

$$N_s\left(\frac{\partial m_p}{\partial t} + \boldsymbol{u} \cdot \nabla m_p\right) = N_s \frac{\mathrm{D}m_p}{\mathrm{D}t} = w_s \quad (13)$$

where $\mathrm{D}m_p/\mathrm{D}t$ is the material or Lagrangian derivative of m_p with respect to time. For spherical particles, this equation may be written in terms of the soot particle radius as

$$N_s 4\pi r_s^2 \rho_p \frac{\mathrm{D}r_s}{\mathrm{D}t} = w_s \quad (14)$$

The material derivative represents the time rate of change following the fluid particle; hence, it is clear that Dr_s/Dt in Eq. (14) is the same as dr_s/dt in Eq. (4), and we can write

$$\frac{\partial r_s}{\partial t} + \boldsymbol{u} \cdot \nabla r_s = \frac{dr_s}{dt} \tag{15}$$

$$w_s = N_s 4\pi r_s^2 \rho_p \frac{dr_s}{dt} \tag{16}$$

The value of dr_s/dt is determined from Hiers's[8,9] soot oxidation model Eq. (8).

In summary, the continuum overlay solution for soot is computed in two parts: In the first part, N_s is found by solving Eq. (12). In the second part, r_s is found by solving Eq. (15). These equations are independent and may be solved in any order. The method can be modified to account for both particle velocity and temperature variations relative to the plume flow, but such modifications will lead to a coupling of the resulting equations and some loss of simplicity. The continuum approach has the advantage that standard Eulerian methods can be utilized to provide very efficient computation of N_s and r_s. In the next section, the specific numerical implementation used in this work is presented.

B. Numerical Implementation

In the present work, an axisymmetric computation of the plume flow was performed with the GASP code.[14] The plume solution was assumed to be steady. The overlay governing equations for steady, axisymmetric flow can be written as

$$\frac{\partial}{\partial x}(N_s u_x) + \frac{\partial}{\partial r}(N_s u_r) + \frac{N_s u_r}{r} = 0 \tag{17}$$

$$u_x \frac{\partial r_s}{\partial x} + u_r \frac{\partial r_s}{\partial r} = \frac{dr_s}{dt}(T, \rho_{O_2}) \tag{18}$$

where x is the axial direction; r is the radial direction; u_x and u_r are plume velocity in the axial and radial directions, respectively; and temperature T and oxygen density ρ_{O_2} of the plume gas are functions of the spatial position. Equations (17) and (18) are approximated numerically by using a second-order upwind difference in the axial direction and a second-order central difference in the radial direction. The values of N_s and r_s are specified at the upstream boundary, whereas extrapolation boundary conditions are used on the radial boundaries. This discretization results in a tridiagonal matrix representing the implicit solution for each radial line, which is computed using the Thomas algorithm (see Ref. 17). The overlay solution proceeds from the upstream boundary to the downstream boundary by marching in the axial direction. The soot number density was specified to be zero outside the plume at the upstream boundary, whereas the soot particle radius was specified to be uniform everywhere on the upstream boundary. (Recall that the combination of N_s and r_s is required to determine the soot fluid density ρ_s.) This numerical algorithm proved to be extremely simple to implement and very fast; however, some numerical oscillations were apparent in the numerical solutions. Because the plume solution contains numerous shocks and sharp gradients, a limiter[18] was also implemented to regulate the maxima and minima in the flowfield.

Large solution first differences such as $u_{i+1} - u_i$ often indicate shocks, but note that "large" and "small" are relative terms, and, traditionally, the reference for a large or small first difference is the neighboring first difference, which is what is used in the implementation. Two possible relative measures used are the following ratios of solution differences:

$$r_i^+ = \frac{u_i - u_{i-1}}{u_{i+1} - u_i}, \qquad r_i^- = \frac{u_{i+1} - u_i}{u_i - u_{i-1}} \tag{19}$$

The ratios have the following cases:

1) The case $r_i^{\pm} \geq 0$ exists if the solution is monotone increasing or monotone decreasing.

2) The case $r_i^{\pm} \leq 0$ exists if the solution has a maximum or a minimum.

3) The case $|r^+|$ is large and $|r^-|$ is small exists if the solution difference decreases dramatically from left to right, or if $u_{i+1} \approx u_i$. In this case, to limit the gradient, r^+ is put equal to $r^+ = (u_{i+1} - u_i)(u_i - u_{i-1})/\delta$ where $|u_{i+1} - u_i| < \delta$.

4) The case $|r^-|$ is large and $|r^+|$ is small exists if the solution difference increases dramatically from left to right, or if $u_{i-1} \approx u_i$. In this case, to limit the gradient, r^- is put equal to $r^- = (u_i - u_{i-1})(u_{i+1} - u_i)/\delta$ where $|u_i - u_{i-1}| < \delta$.

The bounds are imposed on $r^{\pm}$, and this limiting is used to regulate the maxima and minima in the solution regardless of whether they are associated with shocks or not. The accuracy of the overlay method was determined by computing the soot mass flow rate through cross sections normal to the plume axis. Mass flow rate was found to be conserved to within 1%.

IV. Plume Flow Computation

The plume flow used for the subsequent continuum overlay soot computations and radiation calculations is an axisymmetric single-nozzle equivalent of the three-plume Atlas system with gaseous species only. The solutions are obtained for the freestream conditions representative of 21-, 30-, and 40-km altitudes. Inflow conditions at the nozzle exit plane and freestream ambient conditions in the three cases are listed in Tables 1 and 2. The exhaust gases from the Atlas kerosene/LOX motor consist primarily of H_2O, CO, CO_2, and H_2. Because of the high temperature at the nozzle exit and in the shear layer, chemical reactions occur in the gaseous mixture. Including the freestream gases N_2, O_2, and CO_2 and reaction products, a nine-species mixture is used in the flow calculations. A set of five exchange and five recombination reactions have been used in the calculations (Table 3).[19]

The numerical solution of the Reynolds-averaged Navier–Stokes equations for a chemically reacting gas flow was obtained with finite volume spatial discretization on a structured three-dimensional grid implemented in GASP.[14] To capture the flow

Table 1 Flow conditions

Location	Velocity, m/s	Pressure, Pa	Temperature, K
Freestream			
21 km	700	4,790	212
31 km	1,200	1,005	231
40 km	1,476	277	215
Nozzle			
Single nozzle	2,960	68,850	2,230

Table 2 Mole fractions of chemical species

Species	Nozzle	21 km	30 km	40 km
H_2	0.14180	0.00000	0.00000	0.00000
O_2	0.00002	0.21160	0.21146	0.21027
H_2O	0.35202	0.00000	0.00000	0.00000
H	0.00295	0.00000	0.00000	0.00000
O	0.00002	0.00000	0.00000	0.00000
OH	0.00109	0.00000	0.00000	0.00000
N_2	0.00000	0.78839	0.78777	0.78942
CO	0.34233	0.00000	0.00000	0.00000
CO_2	0.15979	0.00000	0.00007	0.00030

Table 3 Chemical reactions[a]

$OH + H_2 \leftrightarrow H_2O + H$
$OH + OH \leftrightarrow H_2O + O$
$OH + O \leftrightarrow H + O_2$
$O + H_2 \leftrightarrow OH + H$
$H + H + M \leftrightarrow H_2 + M$
$H + O + M \leftrightarrow OH + M$
$H + OH + M \leftrightarrow H_2O + M$
$O + O + M \leftrightarrow O_2 + M$
$CO + OH \leftrightarrow CO_2 + H$
$CO + O + M \leftrightarrow CO_2 + M$

[a]M can be any of the chemical species.

properties, it is necessary to have dense grids close to the nozzle and the plume axis with grid density decreasing radially outward. This is required to capture the barrel shock reflections and the shear layer mixing properly. At the lower altitudes, the plume is more compact, and the barrel shock reflection point is closer to the nozzle. Hence, the grid used for the 21-km case is 15 m in the radial extent and 300 m in the axial directions. Because the plume expands more at the higher altitudes of 30 and 40 km, the computational grid is extended 30 m radially for these cases. The resolution of the fine grid in all of the grids is approximately 10 cm. GASP allows various levels of coarsening of a fine grid loaded in memory. For plume radiation predictions to be more accurate, the turbulence effects also have to be modeled as shown by Candler et al.[20] The high Reynolds number κ–ϵ turbulence model is used in all of the calculations. The value of turbulence intensity chosen for the calculations is 0.05. The ratio of eddy viscosity to laminar viscosity at the jet exit is taken in the range of 10, and for the freestream it is 0.1. Candler et al.[20] have shown that κ and ϵ have threshold values and that after a certain value the level of turbulence does not necessarily increase, which, in turn, means that the shear layer does not keep getting thicker because of turbulent mixing. Initially, for all of the calculations, a coarse grid is used, and space marching is performed in the domain to get a quick solution across the whole grid. Space marching is justified because most of the velocities are supersonic, and, thus, little information travels upstream. Global iterations are then performed on the grids in succession, with the information being extrapolated to the next finer grid in sequence when it has converged on the current grid. The purpose of sequencing the grids is to accelerate the solution convergence. Achieving a steady-state solution on a coarse grid is much faster than trying to compute the solution directly on a fine grid. This process ensures that one obtains a solution that is grid and time converged. As shown by Candler et al.,[20] increasing grid fineness also increases turbulence levels.

Viscous derivative terms in the momentum conservation equation are computed with second-order accuracy. For space marching, a second-order fully upwind flux calculation is used. In the case of global iterations, for calculating fluxes, the primary scheme used is van Leer flux vector splitting. The higher-order pointwise reconstruction of the state variables at the cell faces (in a finite volume calculation) is performed using the MUSCL approach. The spatial accuracy of the reconstruction is controlled using a parameter κ. (Note that GASP uses the notation κ, but this is not the κ in the κ–ϵ turbulence model.) The interpolated values of the primitive variables for the left and right state are established by

$$q_{i+\frac{1}{2}}^{\text{left}} = \bar{q}_i + [(1-\kappa)\nabla q_i + (1+\kappa)\Delta q_i] \tag{20}$$

$$q_{i-\frac{1}{2}}^{\text{right}} = \bar{q}_i - [(1+\kappa)\nabla q_i + (1-\kappa)\Delta q_i] \tag{21}$$

where q represents the primitive variable and

$$\Delta q_i = q_{i+1} - q_i, \qquad \nabla q_i = q_i - q_{i-1} \tag{22}$$

The parameter κ may take on values such as $\kappa = -1$ (a second-order and fully upwind scheme), $\kappa = \frac{1}{3}$ (a third-order quadratic reconstruction), and $\kappa = 1$ (central differencing). Therefore, by varying the κ value, the amount of upwinding can be controlled in both the axial and radial directions. The min–mod limiter is used for the fluxes. For the lower-altitude case, a κ value of -0.5 was used to advance the solution. This value increases the degree of upwinding, which can be justified because the velocities are all greater than the sonic velocity.

The origin of the computational grid is defined as the intersection of the plume symmetry axis and the nozzle exit plane. The extrapolation boundary condition is used for all of the boundaries of the grid with the freestream. All three cases are steady-state third-order-accurate Navier–Stokes calculations. The time integration is done using an implicit scheme, primarily Gauss–Seidal iterations, with Courant–Friedrichs–Lewy number values ranging from 0.5 to 20. More information on the schemes and the methods can be found in the GASP manual.[14]

V. Discussion of Results

In this section, we present results of computations performed for the three different altitudes, including testing the sensitivity of our results to the degree of O_2 mixing in the plume and changes in initial distribution of soot particles. In all comparisons, the soot mass flux through the upstream boundary is held constant. For the baseline condition, the soot number density is $N_s = 7.8 \times 10^{14}$ particles/m^3, the soot radius is $r_s = 25$ nm, and the soot is initially distributed uniformly across the nozzle exhaust. These values are also used for any normalizations. The soot number density and size corresponds to a soot mass flow rate of approximately 5% of the total mass flow. Note that, as shown subsequently, the radial scale has been expanded by a factor of two to enhance clarity. The axis labels give the actual radial and axial locations.

A. Plume Flowfields

Figures 1 and 2 compare the temperature and Mach number distribution for the three different altitudes. Note that the

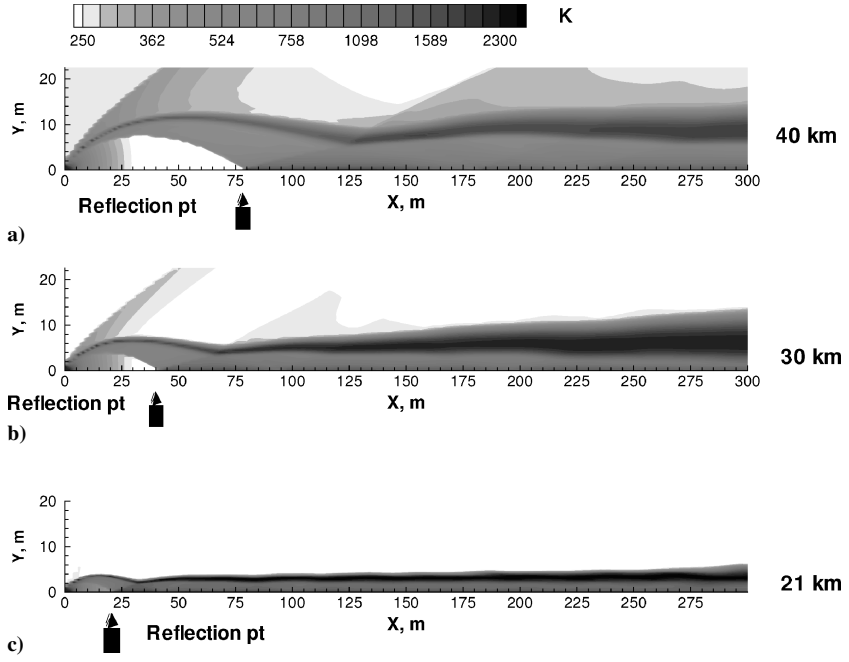

Fig. 1 Comparison of temperature (Kelvin) distribution for a) 40-, b) 30-, and c) 21-km solutions.

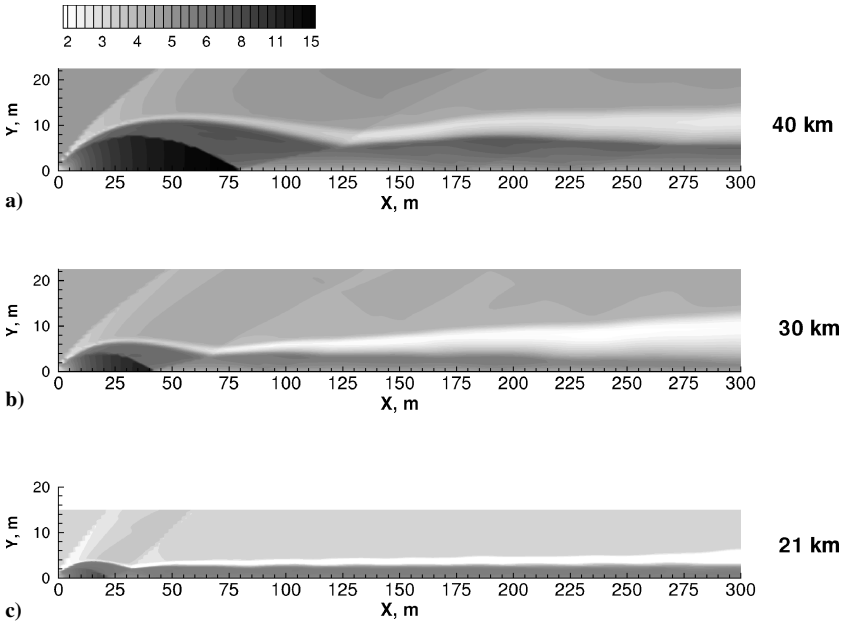

Fig. 2 Comparison of Mach number distribution for a) 40-, b) 30-, and c) 21-km solutions.

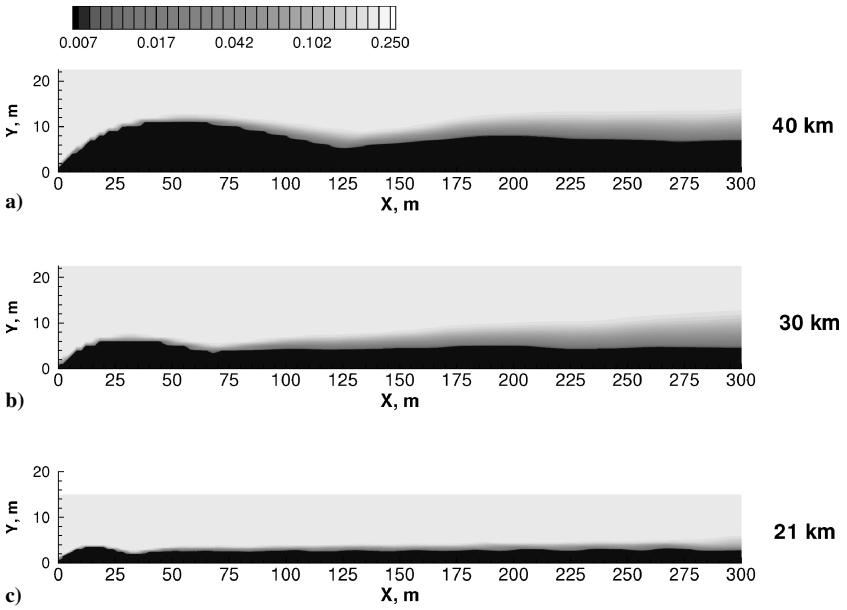

Fig. 3 Comparison of oxygen mole fraction distribution for 40-, 30-, and 21-km solutions.

high-temperature region at the edge of the plume identifies the shear layer for all three altitudes. As expected, for the higher altitude, 40 km, there is more expansion and the plume is wider as compared to the lower altitudes such as 21 km, for which the plume is very compact. In the 30- and 21-km cases, it can be seen that the temperatures in the shear layer are significantly higher than that at 40 km, and also the high-temperature region is found to spread to the whole plume far downstream for the lower altitudes. The flow velocity in the shear layers is less than that of the core of the plume. This is evident from Fig. 2, where the Mach number drops to 2 or 3 in the shear layer as opposed to higher values for the rest of the plume. Again, the steep gradient of velocity across the barrel shock can be seen for the three altitudes and helps to identify the plume length.

The plume length L_{pl}, according to Eq. (2), is calculated for the equivalent Atlas II booster in Table 4, assuming a chamber pressure of 1, 949, 970 Pa at each altitude and a nozzle diameter of 2 m. The chamber pressure is calculated from the values at the exit for the equivalent nozzle, assuming isentropic flow. The simulated values and the plume length formula, given by Morris et al.,[4] Eq. (2),

Table 4 Plume lengths

Altitude, km	Ambient pressure, Pa	Plume length, m, Eq. (2)	Simulation length, m
21	4790	40	20
31	1005	88	40
40	278	167	80

seems to differ by a factor of almost one-half. The simulated plume length can be gauged from Fig. 1, where the barrel shock, which can be identified by its shape and steep temperature rise across it, and its point of intersection with the plume axis is distinctly visible. The higher temperatures and the slowing down of the flow in the shear layer is conducive to chemical reactions, whereas the chemical composition in the core of the plume does not change much. Therefore, the amount of mixing that occurs in the shear layer is also very important. In particular, a finite amount of atmospheric oxygen mixing into the shear layer is required for combustion of soot as given by Eq. (5). The turbulence model is important to simulate the mixing in the shear layer for all three altitudes. Figure 3

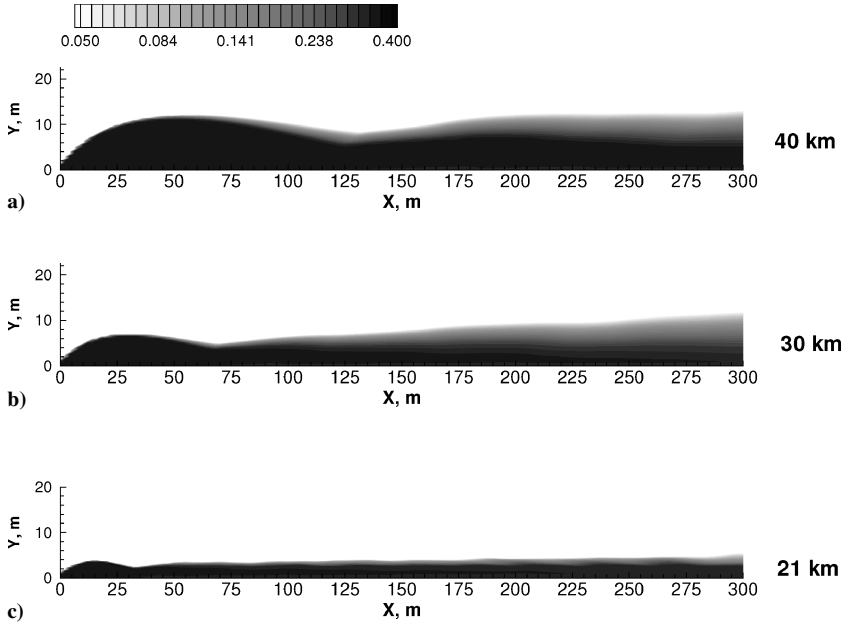

Fig. 4 Comparison of water mole fraction distribution for 40-, 30-, and 21-km solutions.

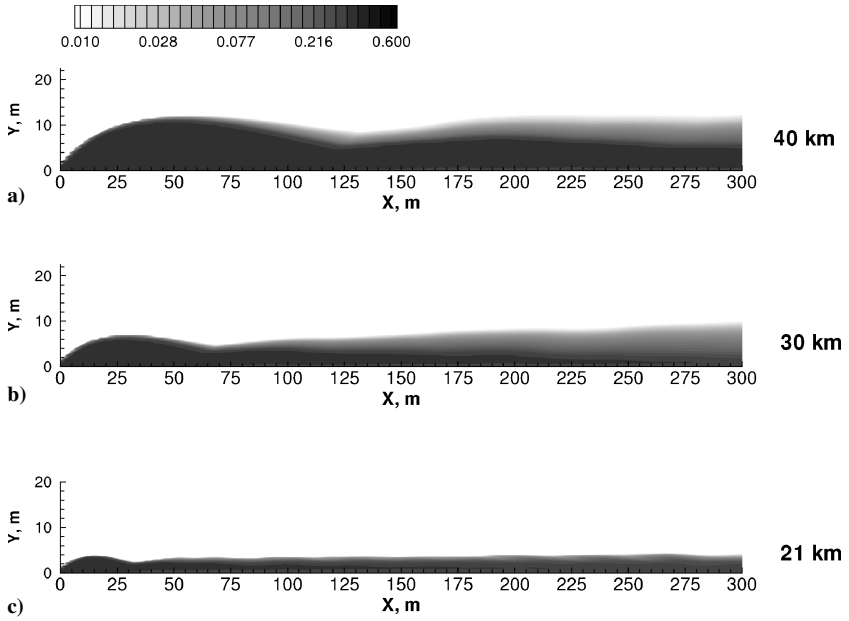

Fig. 5 Comparison of CO mole fraction distribution for 40-, 30-, and 21-km solutions.

shows the change in O_2 mole fraction, or penetration, into the shear layer as a function of altitude. Note that there is greater mixing at the altitudes higher than 21 km, but it should be noted that this does not necessarily mean that the higher altitudes have more oxygen for combustion because there is a significant difference in the density of oxygen. The density of oxygen at 21 km is 20 times greater than that at 40 km and 5 times greater than that at 30 km. Thus, even though there is less mixing at 21 km, there is more oxygen availability for soot combustion. Figures 4 and 5 show how the mole fraction of H_2O and CO, the two main chemical species at the nozzle exit, change in the plume. For both species, the change in mole fraction is seen only in the plume shear layer. As discussed in earlier work,[7] water dissociates to form OH in the high-temperature regions of the shear layer, whereas its mole fraction in the plume core remains essentially unchanged. The carbon monoxide concentration decreases due to the last reaction in Table 3.

B. Soot Overlay Results

The normalized number density of soot is shown in Fig. 6. Normalized quantities in the paper refer to the value at any point divided by the value of the quantity at the nozzle exit. The soot concentration is higher at the lower altitude, whereas for the higher-altitude case, the soot particles are distributed over a much larger volume. This is a consequence of that, in the absence of combustion, the mass flux of soot through any plane crossing the plume is constant, and so, in the more underexpanded case (40 km), due to the larger plume cross section, the number density of soot decreases. This is understood if we consider a control volume surrounding the computational domain. The mass flux of soot in should equal the mass flux of soot out when there is no combustion. No flow crosses the axisymmetric axis, and at the cylindrical outer boundary, the transverse velocities are negligible. Hence, the mass flux of soot across any downstream plane is constant without combustion. Note that, in

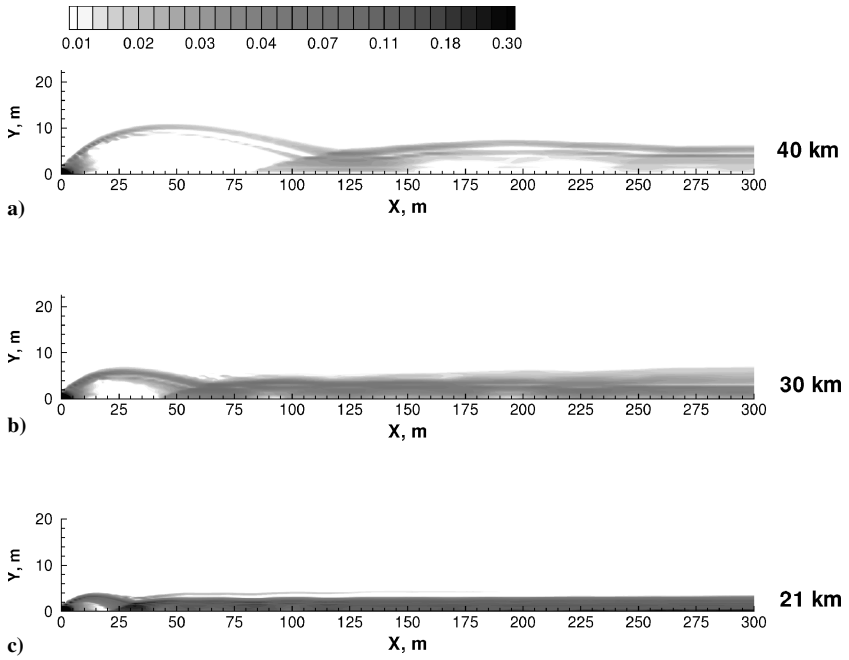

Fig. 6 Comparison of normalized soot number density for 40-, 30-, and 21-km solutions.

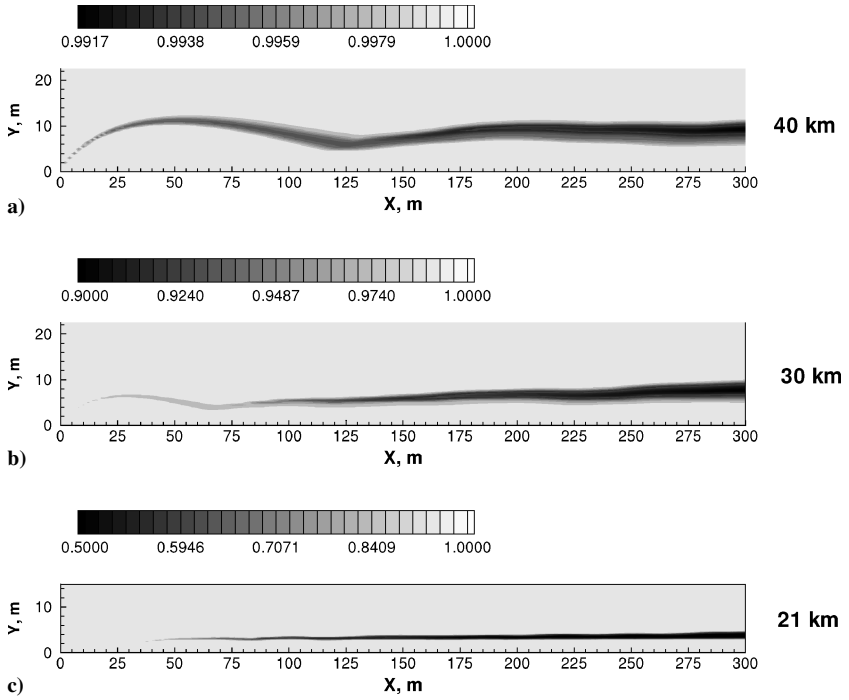

Fig. 7 Comparison of normalized soot radii distribution for 40-, 30-, and 21-km solutions.

Fig. 6, there is no generation or destruction of soot. It simply shows how the soot would be distributed in the absence of combustion. At 40 km (Fig. 6a) it appears that at 80–150 m downstream there is suddenly more soot than before. This is the region after the shock where the velocity slows down and where there is an increase in density. Hence, the number density increases. It has been observed that the soot velocity and soot temperature do not differ significantly from the plume gas flow, and the soot is assumed to have the same velocities as the background flow in the overlay method.

An indication of soot combustion is the change in radii of the soot particles. Figure 7 shows a comparison of the normalized soot particle radius. A normalized value of one indicates that the radius is unchanged from the initial baseline value, that is, no combustion, whereas a value of zero indicates that complete combustion has occurred. The value of r_s is computed everywhere, even if there are no soot particles at a particular spatial position. This is a result of the separation of the N_s and r_s computations in the continuum overlay method. Hence, we can tell where soot would oxidize if particles were indeed present. Examination of Fig. 7 shows that the normalized soot radii change in the shear layer where the presence of oxygen, higher temperatures, and slower moving gases allow combustion to take place. Note that the color scale for the radii at the different altitudes are different because, at 40 km, there is a much smaller change in the radii as compared to that at 21 km. Combining the number density plot and the radii plot gives the actual mass soot density (Fig. 8). From Fig. 8, it is obvious that the soot density is

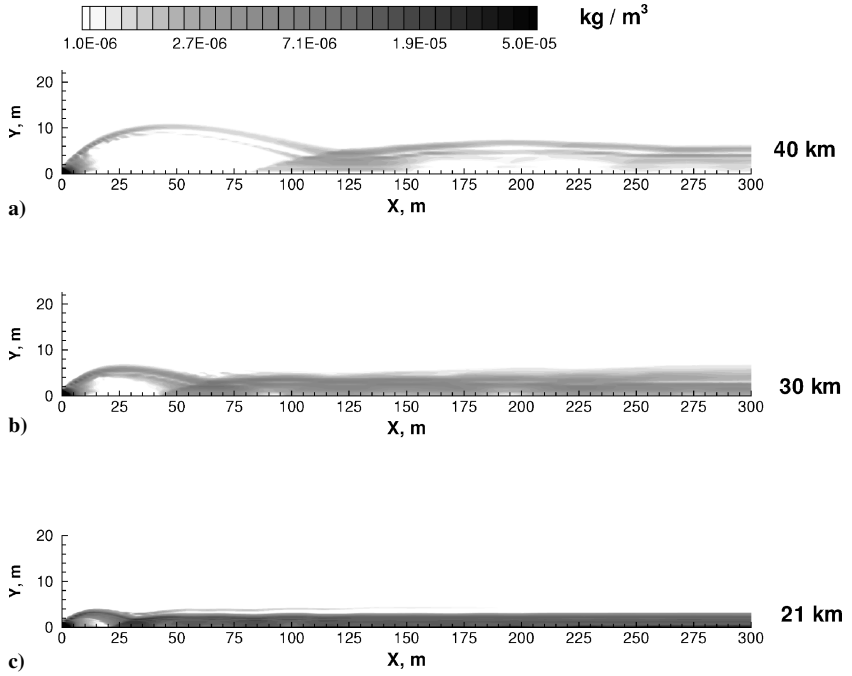

Fig. 8 Comparison of soot mass density distribution for 40-, 30-, and 21-km solutions.

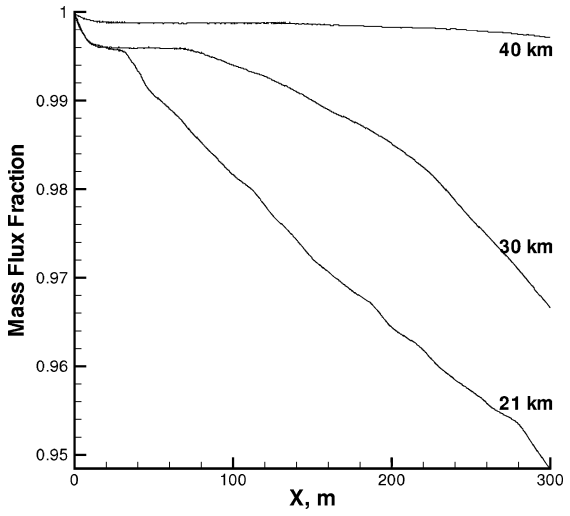

Fig. 9 Mass flux fraction of soot at 40, 30, and 21 km.

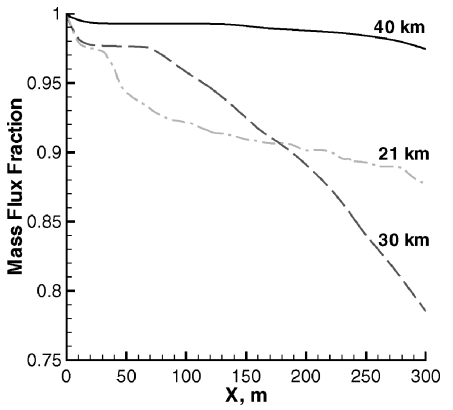

Fig. 10 Mass flux fraction of soot at 40, 30, and 21 km for the O_2 concentration increased by a factor of 10.

at a maximum near the nozzle. Even with more combustion at the lower altitude, the soot density at 21 km is greater than the density at 40 km. This seems counterintuitive because there is more mixing of oxygen into the shear layer at the lower altitude due to the higher concentration of oxygen and, hence, increased combustion at the lower altitude. This is again due to the difference in number density distribution of soot at the two altitudes. To demonstrate that the total mass of soot is indeed lower, due to oxidation, the mass flux of soot through planes perpendicular to the plume has been computed as a function of downstream distance in Fig. 9. Figure 9 shows the mass flux fraction (mass flux after combustion/mass flux in absence of combustion). Thus, at 40 km, there is very little combustion, that is, the mass flux ratio deviates little from one, whereas at 21 km, the mass flux decreases by 5%. This verifies that even though the soot density is greater at 21 km, combustion is much greater at lower altitudes, and the density variation is mainly due to soot being distributed over a larger region at 40 km. The soot density at 20 km compares favorably with the 15-km computation in Ref. 13.

C. Excursions from the Baseline Model

To further demonstrate the utility of the soot overlay method, we next examine the sensitivity of the model to two important factors in this work: 1) uncertainties in the plume flowfield solution and 2) possible variations in the initial soot spatial distribution at the nozzle exit plane.

As discussed earlier, the modeling of the plume flow is difficult due to numerical as well as physical issues, such as turbulence. The uncertainty in the degree of soot combustion due to turbulence and grid requirements in these flows is difficult to access. We can estimate the sensitivity of soot combustion in the plume due to the turbulence model and its associated numerical issues by increasing the molecular oxygen concentration in the steady-state plume solution by a factor of 10. This factor is more than adequate to account for better oxygen mixing in the plume shear layer that might be obtained with a true, three-dimensional turbulence model. Figure 10 presents the mass flux fraction, calculated in a manner similar to Fig. 9. A comparison of Figs. 9 and 10 shows that with increased available molecular oxygen the degree of soot combustion increases at all three altitudes. In contrast to the baseline plume flow model, Fig. 9, however, the increase in combustion with freestream number density is not monotonic. We cannot conclude that the rate of combustion at 30 km would actually be higher than that at 21 km.

Instead, we observe that the lower-altitude solution is less sensitive to uncertainties in the molecular oxygen concentration and, hence, the degree of mixing due to turbulence in the flowfield. Consistent with Fig. 3, we find that at 30 km the plume flowfield is more oxygen limited than at 21 km, whereas at 40 km the soot oxidation rate is so low that any uncertainties in the O_2 mixing is unlikely to change the steady-state soot concentration.

The initial examination of the baseline computation indicated that the most likely place for soot combustion was in the plume shear layer. This is reasonable because mixing of O_2 from the freestream coupled with the high shear-layer temperature ensures that the soot can oxidize most easily at the edge of the plume. Furthermore, if the fuel mixture is richer toward the nozzle wall, it would be likely that the soot distribution may not be uniform across the nozzle exit plane.

Three calculations were performed for the 21-km case with the soot redistributed at the nozzle exit plane, that is, the overlay upstream boundary, to investigate the sensitivity of the computations to the initial spatial distribution: 1) the soot distributed radially from 0.8 to 1.0 m, that is, all of the soot particles near the nozzle wall; 2) the soot distributed radially from 0.8 to 1.6 m (0.6 m beyond the nozzle wall); and 3) the soot distributed from the centerline to 0.6 m beyond the nozzle radius. In each case, the total soot mass flux was held constant by adjusting the soot number density at the nozzle exit plane. Figure 11 shows the computed downstream spatial distribution of soot fluid density for the three different initial conditions. There are clearly differences between the solutions, most notably in Fig. 11a, where the initial soot density was highest as expected and, therefore, the longest persisting, whereas for the other initial distributions the density is visibly lower, but it is difficult to interpret from Figs. 11 how much of the soot change in density is due to combustion.

For this reason, we also plot the instantaneous rate of change of soot density with respect to time due to combustion in Fig. 12,

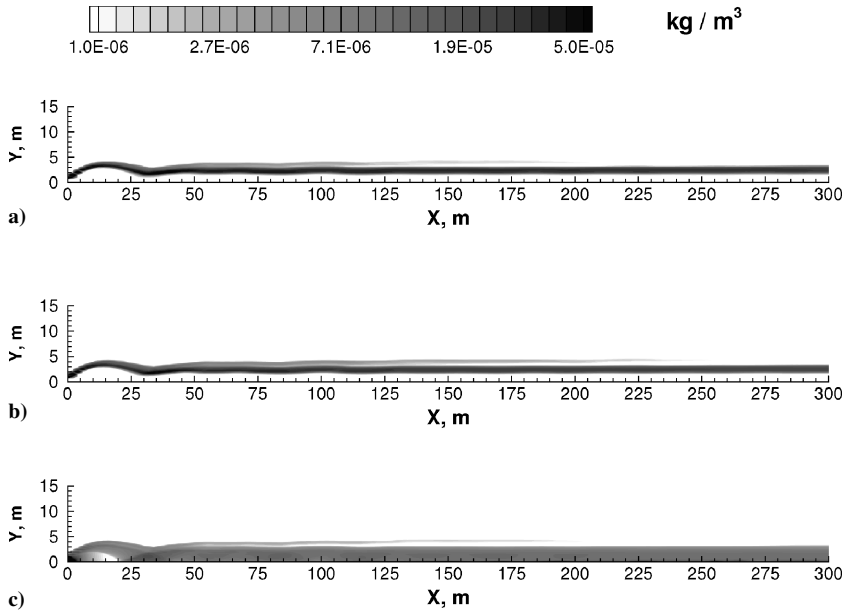

Fig. 11 Comparison of the soot density ρ_s (kilograms per cubic meter) for three constant soot mass flux upstream boundary conditions for a nozzle with 1-m radius: a) soot concentrated between 0.8 and 1.0 m, b) soot concentrated between 0.8 and 1.6 m, and c) soot distributed from the centerline to 1.6 m at 21 km.

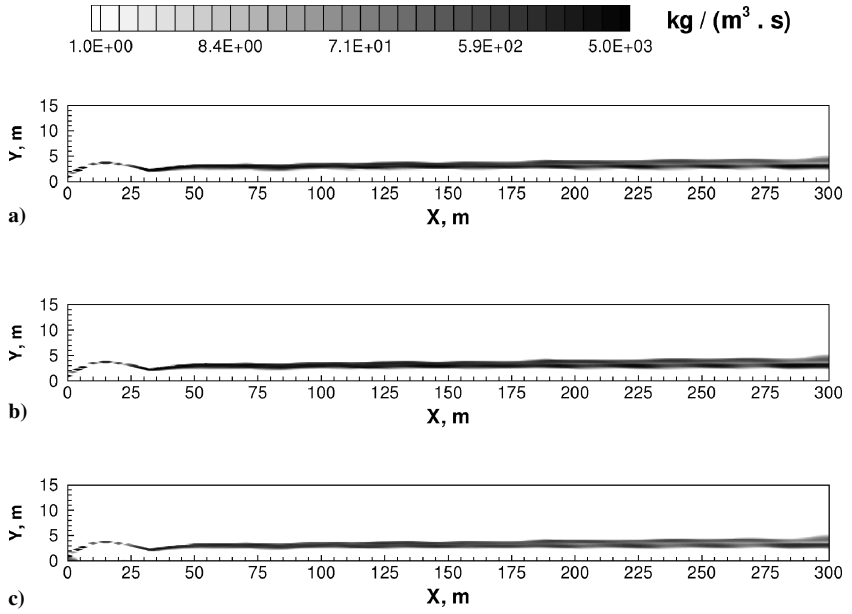

Fig. 12 Comparison of the instantaneous change in density due to combustion $-w_s$ (kilograms per cubic meter second) for three constant soot mass flux upstream boundary conditions for a nozzle with 1-m radius: a) soot concentrated between 0.8 and 1.0 m, b) soot concentrated between 0.8 and 1.6 m, and c) soot distributed from the centerline to 1.6 m at 21 km.

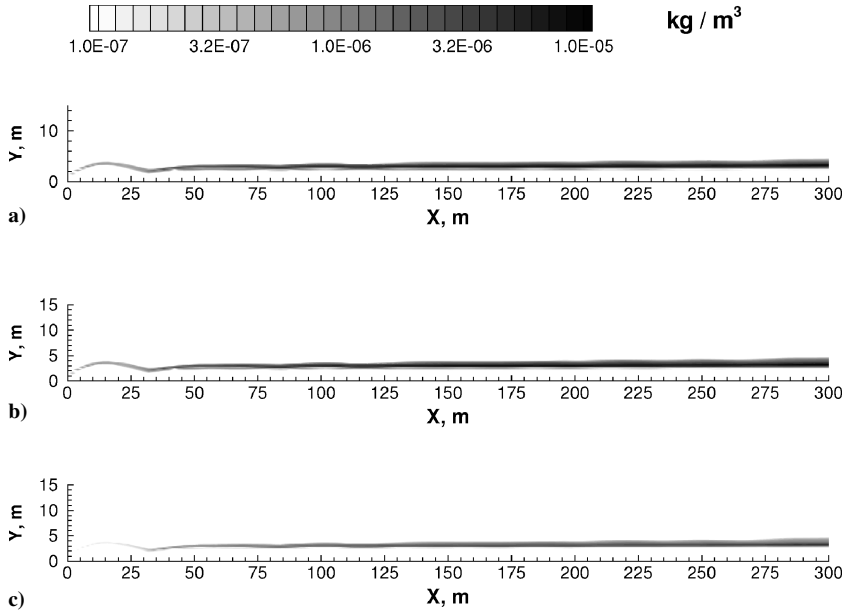

Fig. 13 Comparison of change in soot density (kilograms per cubic meter) due to combustion for three constant soot mass flux upstream boundary conditions for a nozzle with 1-m radius: a) soot concentrated between 0.8 and 1.0 m, b) soot concentrated between 0.8 and 1.6 m, and c) soot distributed from the centerline to 1.6 m at 21 km.

that is, the source term w_s defined in Eq. (16), and the change in soot density due to combustion in Fig. 13 (determined by subtracting ρ_s from the value of ρ_s computed with w_s set to zero). Both Figs. 12 and 13 show that soot concentrated near the wall of the nozzle combusts more readily because most of it gets transported into the shear layer. Even at 21 km, the soot distributed from the centerline to 1.6 m, Figs. 12c and 13c, has lower soot density and, hence, less combustion, whereas for higher altitudes it will decrease even more.

VI. Conclusions

In this paper, we have presented the continuum approach for the soot overlay problem. The second-order continuum overlay approach has the advantage that it decouples the calculation of the soot number density and the soot particle radius, and standard Eulerian methods can be utilized to provide very fast and efficient computation of these two quantities. Through comparison of results for different initial distributions, it has been demonstrated that the soot overlay method is capable of predicting variations in the soot particle distribution due to combustion.

A number of important future research directions are suggested by this preliminary effort. The continuum overlay method is computationally efficient compared to other methods like the DSMC approach. However, to be useful for operational considerations, it needs to be extended to three dimensions. The variation in the soot combustion and spatial distribution with altitude is also consistent with the midwave-infrared spectral data of a recent Atlas launch.[21] With the steady-state particle flowfields, the particle size, temperature, and concentration spatial distribution can be used in future work to calculate the plume radiation due to particulate thermal emission as well as solar illumination.

Acknowledgments

The research at Pennsylvania State University was supported by the Space and Naval Warfare Systems Center San Diego Grant DUNS 04-399-0498 and U.S. Army Research Offfce Grant DAAG55-98-1-009. These programs are supported by the Science and Technology Directorate of the Missile Defense Agency, which is conducting programs to characterize and measure the optical radiation from rocket plumes with high spatial resolution. We would like to thank specifically Robert S. Hiers III for his valuable comments and suggestions throughout the work. Finally, we wish to acknowledge the significant assistance we received from Alina A. Alexeenko in using GASP.

References

[1]Simmons, F. S., *Rocket Exhaust Plume Phenomenology*, Aerospace Press, AIAA, 2000, ISBN 1-884989-08-X.

[2]Moran, J. P., "Similarity in High-Altitude Jets," *AIAA Journal*, Vol. 5, No. 7, 1967, pp. 1343–1345.

[3]Bannik, W., Houtman, E. M., and Bakker, P. G., "Base Flow/Underexpanded Exhaust Plume Interaction in a Supersonic External Flow," AIAA Paper 98-1598, April 1998.

[4]Morris, N., Buttsworth, J. T., and Brescianini, C., "An Experimental and Computational Study of Moderately Underexpanded Rocket Exhaust Plumes in Coflowing Hypersonic Freestream," AIAA Paper 95-6127, 1995.

[5]Genkin, L., Baer, M., and Falcovitz J., "MOC Computation of Intermediate-Altitude Rocket Plumes with Shock Waves," AIAA Paper 96-1883, 1983.

[6]Ebrahimi, H. B., Levine, J., and Kawasaki, A., "Numerical Investigation of Twin-Nozzle Rocket Plume Phenomenology," *Journal of Propulsion and Power*, Vol. 16, No. 2, 2000, pp. 178–186.

[7]Alexeenko, A. A., Gimelshein, N. E., Levin, D. A., Collins, R. J., Candler, G. V., Gimelshein, S. F., Hong, J. S., and Schilling, T., "Modeling of Flow and Radiation in the Atlas Plume," *Journal of Thermophysics and Heat Transfer*, Vol. 16, No. 1, 2003, pp. 50–57.

[8]Hiers, R. S., III, "Rarefaction Effects in Small Particle Combustion," Ph.D. Dissertation, Univ. of Tennessee, Knoxville, Aug. 1997.

[9]Hiers, R. S., III, "Critical Behavior in Small Particle Combustion," *Journal of Thermophysics and Heat Transfer*, Vol. 14, No. 1, 2000, pp. 53–58.

[10]Plastinin, Yu., Karabadzhak, G., and Khmelinin, B., "Ultraviolet, Visible and Infrared Spectra Modeling for Solid and Liquid Fuel Rocket Exhausts," AIAA Paper 2001-0660, 2001.

[11]Karabadzhak, G., Plastinin, Yu., and Rodionov, A., "Soot Oxidation Modeling in Plume," AIAA Paper 2001-3858, 2001.

[12]Plastinin, Yu., Karabadzhak, G., Khmelinin, B., Baula, G., and Rodionov, A., "Advanced Model for Soot Radiation in the Plume," AIAA Paper 2002-0798, 2002.

[13]Brentner, K. S., Gimelshein, S. F., Levin, D. A., and Viswanath, K., "Investigation of Soot Combustion in Underexpanded Jet Plume Flows," AIAA Paper 2003-0506, Jan. 2003.

[14]*GASP Version 3, The General Aerodynamic Simulation Program, Computational Flow Analysis Software for the Scientist and Engineer, User's Manual*, Aerosoft Co., Blacksburg, VA, 1996.

[15]Wolfhard, H. G., and Garcia, K. K., "Carbon Formation in Rocket Combustion," *Proceedings of the IRIS Targets, Backgrounds, and Discrimination*, Vol. 2, ERIM Rept. 213400-129-X(II), 1992.

[16]Levin, D. A., Candler, G. V., and Collins, R. J., "Overlay Method for Calculating Excited State Species Properties in Hypersonic Flows," *AIAA Journal*, Vol. 35, No. 2, 1997, pp. 288–294.

[17]Tannehill, J. C., Anderson, D. A., and Pletcher, R. H., *Computational Fluid Mechanics and Heat Transfer*, 2nd ed., Taylor and Francis, Washington, DC, 1997.

[18]Laney, C. B., *Computational Gasdynamics*, Cambridge Univ. Press, New York, 1998, IBSN 0521570697.

[19]Hong, J. S., Levin, D. A., Collins, R. J., Emery, J., and Tietjen, A., "Comparison of Atlas Ground Based Plume Imagery with Chemically Reacting Flow," AIAA Paper 97-2537, June 1997.

[20]Candler, G., Rao, R., and Levin, D., "Numerical Simulations of Atlas II Rocket Plumes," AIAA Paper 2001-0354, Jan. 2001.

[21]Barton, P., Pearce, B., Freeman, N., Tietjen, A., Emery, J., Dawson, D., Wendt, J., Moyers, R., Hiers, R., and Lovern, M., "Atlas Spectral Imagery Data and Mechanisms," AIAA Paper 2001-1121, Jan. 2001.